



Contents lists available at ScienceDirect

Experimental Thermal and Fluid Science

journal homepage: www.elsevier.com/locate/etfs

Characterizing combustion of a hybrid rocket using laser absorption spectroscopy

Sihan Fang^{a,b}, Zezhong Wang^{a,b}, Xin Lin^{a,*}, Fei Li^{a,**}, Renjie Li^{a,b}, Jing Li^{b,c}, Zhedian Zhang^{b,c}, Yan Liu^{b,c}, Xilong Yu^{a,b}

^a State Key Laboratory of High Temperature Gas Dynamics, Institute of Mechanics, Chinese Academy of Sciences, Beijing 100190, China

^b School of Engineering Science, University of Chinese Academy of Sciences, Beijing 100049, China

^c Key Laboratory of Advanced Energy and Power, Institute of Engineering Thermophysics, Chinese Academy of Sciences, Beijing 100190, China

ARTICLE INFO

Keywords:

Tunable diode laser absorption spectroscopy
Hybrid rocket motor
Temperature
Partial pressure
Combustion efficiency

ABSTRACT

The combustion of an oxygen/paraffin hybrid rocket motor was experimentally characterized. Firing tests were conducted for different oxidizer mass fluxes ranging from 2.47 to 3.40 g/(cm²·s). Variations in temperature and H₂O partial pressure at the nozzle exit were diagnosed using mid-infrared tunable diode laser absorption spectroscopy (TDLAS) based on H₂O absorption near 2.5 μm. Three H₂O absorption lines were simultaneously covered by only one distributed feedback (DFB) laser using scanned-wavelength direct absorption (DA) mode with 2.0 kHz repetition rate. Measurement uncertainty was analyzed in detail considering line-strength uncertainty and Voigt fitting residuals. A two-dimensional (2D) model of the nozzle was constructed using the ANSYS FLUENT CFD software package. The combustion efficiency of the hybrid rocket motor was evaluated from the perspectives of chemical reaction and heat release, respectively, based on TDLAS results and CFD simulations. The effectiveness of the evaluation was validated by comparing its results with characteristic velocity (C*)-based combustion efficiency. Finally, comparisons of combustion efficiencies among different cases show that increasing the oxidizer mass flux or oxidizer-to-fuel ratio improves the combustion efficiency of the hybrid rocket motor under our experimental conditions.

1. Introduction

The hybrid rocket motor, typically containing liquid oxidizer and solid fuel, has the advantages of high reliability, multiple restart capability, high safety, and low cost compared with conventional solid- or liquid- propulsion systems [1–4]. These advantages make the hybrid rocket motor important for future aerospace exploration [5,6]. Unfortunately, the diffusive nature of turbulent flames due to its unique structure poses great challenges to combustion diagnosis and limits understanding of its combustion mechanisms [7–10]. Currently, the combustion performance of hybrids is mainly evaluated via the characteristic velocity C^* [11]:

$$C^* = P_c A_{th} / \dot{m} \quad (1)$$

where P_c , A_{th} , and \dot{m} represent the chamber pressure, nozzle-throat area and mass flow rate respectively. Although convenient, the global metrics

in this method provide little granularity to the inherent loss mechanisms that may decrease the overall combustion performance. These limitations have hindered the development of hybrid rocket motors for most practical applications [12]. To advance the understanding of physico-chemical mechanisms governing combustion performance, it is necessary to make quantitative in-situ diagnosis of key flow-field parameters with high fidelity and time resolution in real combustion conditions.

For any chemical-propulsion system, temperature and species partial pressure are the two most important parameters because they reflect most key combustion processes and quantify heat loss. In recent years, numerous non-intrusive optically-based diagnostic methods have been applied to temperature and species partial pressure diagnosis, such as planar laser-induced fluorescence (PLIF), coherent anti-Stokes Raman scattering (CARS), Rayleigh scattering (RS), and tunable diode laser absorption spectroscopy (TDLAS). These spectroscopic methods vary significantly in their accuracy and simplicity [13]. PLIF is a well-established technique for two-dimensional (2D) detection. However,

* Corresponding author.

** Co-corresponding author.

E-mail addresses: linxin_bit@imech.ac.cn (X. Lin), lifei@imech.ac.cn (F. Li).

quantitative interpretation of PLIF signals requires independent information on local quenching rates, which can be difficult or even impossible to obtain in turbulent flames [14]. CARS is well known for strong signal strength and good sensitivity, but it suffers from non-resonant background fluorescence noise and is sensitive to refractive index gradients in the optical path [15,16]. RS has the advantage of high spatial resolution for temperature; however, it is difficult to determine the scattering cross section precisely in reaction flows [17]. Lastly, these three spectroscopic methods are hard to be fiber-coupled and require both bulky light sources and sophisticated laser equipment [14]. These issues and requirements pose significant challenges for highly quantitative and in-situ measurements under the harsh environments of real propulsion systems.

TDLAS is a promising approach to address these practical issues in analyzing reactive flows, and it often serves as an effective tool for quantifying the time-resolved temperature and partial pressure of target gas species [18–23]. Owing to its advantages of non-intrusive detection, high sensitivity, high signal-to-noise ratio (SNR), fast response, robustness, and compactness, TDLAS has been penetrated into the large area of combustion diagnostics of real engines and propulsions such as scramjets [24], internal combustion engines [25], pulse detonation combustors [26], and coal gasifiers [27].

TDLAS technique has recently been adapted to combustion diagnosis of hybrid rocket motors. In 2016, Mohamed et al. used TDLAS to measure temperature and concentration variations at the nozzle exit of a hybrid rocket motor [28]. Later in 2019, Bendana et al. claimed to have obtained the quantitative 2D structure of a hybrid reaction layer based on TDLAS (Strictly speaking, an apparatus without a downstream nozzle is not a hybrid rocket motor, so the combustion environment is significantly different from that of hybrid rockets.) These works have successfully confirmed the potential of TDLAS technology in hybrid motor diagnosis. However, they did not fully use the TDLAS measurements to extract information of reactive flows that may closely relate to combustion mechanisms and help to quantitatively evaluate the combustion performance of hybrid rocket motors.

In this study, we experimentally characterized the combustion performance of a laboratory-scale oxygen/paraffin hybrid rocket motor. Experiments were conducted at different oxidizer mass fluxes from 2.47 to 3.40 g/(cm²·s), corresponding to oxidizer-to-fuel ratios (O/Fs) from 2.77 to 3.18. Variations of temperature and H₂O partial pressure were measured with a mid-infrared TDLAS system near 2.5 μm. Three well-isolated fundamental vibrational transitions (4029.52 cm⁻¹, 4030.51 cm⁻¹ and 4030.73 cm⁻¹) were simultaneously probed by a single distributed feedback (DFB) laser at a 2.0 kHz repetition rate using scanned-wavelength direct absorption (DA) strategy. Measurement uncertainty was analyzed in detail considering Voigt-fitting residuals and line-strength uncertainty. A simplified 2D model was constructed for the nozzle using the ANSYS FLUENT CFD software package. Combining the TDLAS measurement results with CFD simulations, we calculated the combustion efficiency of the hybrid rocket motor from the perspectives of chemical reaction (using H₂O partial pressure) and heat release (using gas temperature), respectively. Results were compared with classical C*-based combustion efficiency to validate the effectiveness of the evaluation. Finally, comparisons were made between firing tests to recognize the effects of O/F and mass flux variations on hybrid combustion performance.

2. Laser absorption spectroscopy

2.1. Absorption theory

Laser absorption spectroscopy is an optical diagnostic technique that exploits the resonance of a coherent laser with the photon energy of a specific molecule [29,30]. The fundamentals of DA spectroscopy have been well described in numerous works [13,17,24,31–36], a brief review is given here to establish terms and units and facilitate the

discussion that follow.

In DA measurements for a uniform gas field, intensity attenuation is described by the Beer–Lambert law:

$$\frac{I_t}{I_0} = \exp(-k_v L) \quad (2)$$

where I_0 and I_t are the incident and transmitted laser intensities, L [cm] is the optical path length, and k_v [cm⁻¹] is the absorption coefficient. For a transition of frequency ν , k_v can be expressed as

$$k_v = P_i \cdot S(T) \cdot \phi(\nu) \quad (3)$$

where P_i [atm] is the partial pressure of the absorption species (here i is water vapor), $S(T)$ [cm⁻²atm⁻¹] the line-strength of the transition, and $\phi(\nu)$ [cm] the line-shape function. Noting that the line-shape function $\phi(\nu)$ is normalized to unity as $\int \phi(\nu) d\nu \equiv 1$, the integrated absorbance A [cm⁻¹] can be determined as:

$$A = \int k_v L d\nu = P_i \cdot S(T) \cdot L \quad (4)$$

According to two-line thermometry [37], the path-averaged gas temperature T can be determined as:

$$T = \frac{\frac{hc}{k} (E_2'' - E_1'')}{\ln R + \ln \frac{S_2(T_0)}{S_1(T_0)} + \frac{hc}{k} (E_2'' - E_1'') / T_0} \quad (5)$$

where R is the ratio of integrated absorbances:

$$R = \frac{A_2}{A_1} \quad (6)$$

A criterion χ_T is defined to monitor the temperature sensitivity of absorption lines and can be approximated as [31]:

$$\chi_T = \left| \frac{dR/R}{dT/T} \right| \approx \frac{hc}{k} \left| \frac{E_1'' - E_2''}{T} \right| = \frac{hc}{k} \frac{|\Delta E''|}{T} \quad (7)$$

The species partial pressure P_{H_2O} can be determined when the gas temperature T [K] is acquired:

$$P_{H_2O} = \frac{\int k_v L d\nu}{S(T) \cdot L} = \frac{A}{S(T) \cdot L} \quad (8)$$

2.2. Line selection

For DA measurement of high-temperature flame created by a hybrid rocket motor, spectroscopic signals can be affected by burning particles and thermal radiation, which decreases the SNR and measurement accuracy. This requires strong absorption signals of transition lines. The fundamental vibrational bands (ν_1 and ν_3) of H₂O [33] are approximately 20 times stronger than the overtone and combination bands [12], which provide the capability for precise measurement at such harsh conditions.

Fig. 1 shows broadband simulations of H₂O, CO, and CO₂ spectra in the near- and mid-infrared at a representative temperature of 2000 K. For H₂O, the strongest vibrational bands with minimal CO and CO₂ interference occur in the fundamental bands near 2.5 and 2.9 μm, which provides spectral windows of well-isolated transitions suitable for TDLAS sensing. The simulated spectra for the four candidate H₂O line pairs (A [41], B [33], C [17], and D [42]) were plotted in Fig. 2, which indicates that CO and CO₂ absorptions have negligible interference with that of H₂O under expected hybrid motor combustion conditions. The relevant spectroscopic parameters for the transitions and source databases are presented in Table 1.

Finally, line pair A near 2.5 μm was selected for the following reasons: (1) line pair A has large absorption strength; (2) the transitions are well isolated; (3) the temperature sensitivity (shown in Fig. 3 (a)) is high enough for combustion diagnosis; (4) low line-strength uncertainty

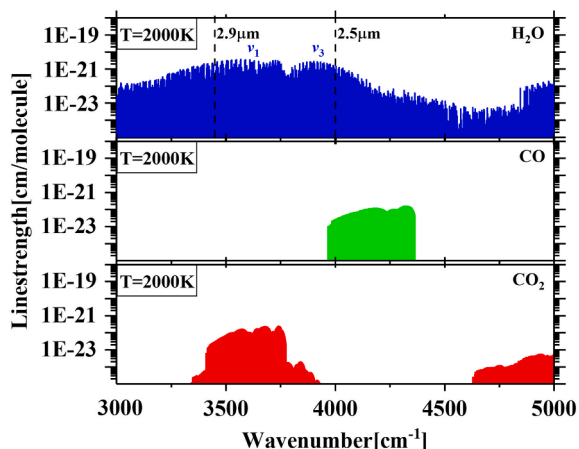


Fig. 1. Line-strengths for the near and mid-infrared bands of H₂O, CO and CO₂ at 2000 K. (Parameters of H₂O and CO₂ come from the HITRAN 2016 database [38], and parameters of CO come from the HITEMP 2019 database [39,40]).

propagated by temperature uncertainty ΔT [43]; (5) relatively large lower state energy ($E'_l > 1500 \text{ cm}^{-1}$ for 2000 K, shown in Fig. 3 (b)) helps ensure high immunity from the ambient colder water vapor. It is noteworthy that the line-strength of line pair A has been validated in a high-temperature (650–1325 K) quartz gas cell [12,42,44,45] (which is considered in uncertainty analysis in Section 4.1), and the ability of line pair A for high temperature ($\sim 1800 \text{ K}$, similar to our temperature condition) diagnosis has been validated on standard flames in Ma's work [41].

3. Experimental setup

The laboratory-scale hybrid rocket motor used for combustion analysis is briefly described here (shown in Fig. 4), and further information on the apparatus can be found in our previous study [46]. This motor used gas oxygen as the oxidizer and pure paraffin as the fuel. The fuel grain was centrifuged into a single port structure 70 mm in length, 30 mm in inner diameter, and 64 mm in outer diameter. The mass flow rate of oxygen was adjusted by a calibrated mass flow controller (Bronkhorst, model F-203AV), and two pressure transducers were placed in the pre-chamber and aft-chamber respectively. A nozzle was attached to the combustor exit to accelerate the reactive flow. The diameters of the nozzle throat and nozzle exit were 5 mm and 12 mm respectively. The entire system was controlled by a computer using the LABVIEW program to simultaneously trigger the TDLAS data acquisition and motor ignition. Event timing for the experiments was set using a National Instruments USB-6211 multi-function unit. Firing tests were

Table 1
Spectroscopic parameters of the candidate transitions.

Line pair	Wavenumber [cm ⁻¹]	Wavelength [nm]	S@296 K [cm ⁻² atm ⁻¹]	E'' [cm ⁻¹]
A ^(a)	4029.52	2481.69	8.50×10^{-5}	2660.94
	4030.51	2481.08	1.80×10^{-9}	4902.61
	4030.73	2480.94	2.15×10^{-9}	4889.49
B ^(a)	3982.06	2511.26	8.99×10^{-3}	1581.34
	3982.75	2510.83	6.24×10^{-7}	3654.05
C ^(a)	3459.73	2890.40	4.02×10^{-6}	3386.38
	3460.59	2889.68	8.85×10^{-4}	2073.51
D ^(a)	3920.09	2550.96	6.49×10^{-1}	704.21
	4030.73	2480.94	2.15×10^{-9}	4889.49

(a) Values taken from HITRAN 2016 database [38].

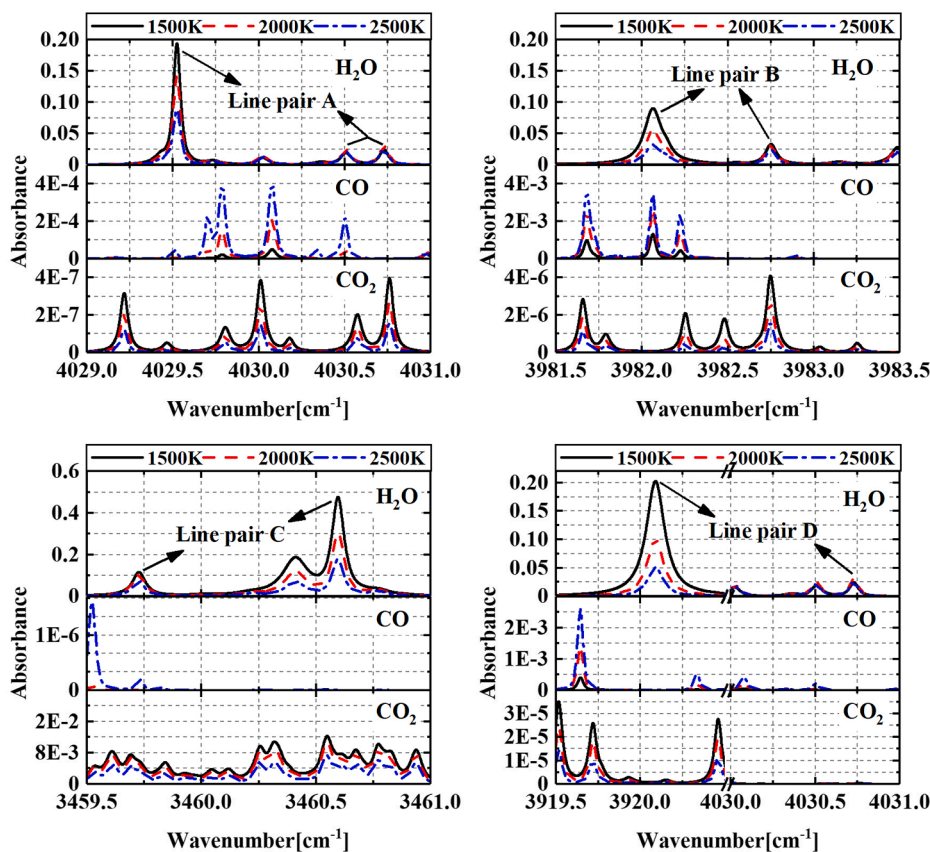


Fig. 2. Absorbance simulation of H₂O transitions for 4 candidate line pairs based on the HITRAN 2016 database and the corresponding CO (HITEMP 2019 database) and CO₂ (HITRAN 2016 database) absorbance were plotted for comparison. $P = 1 \text{ atm}$, $L = 1.2 \text{ cm}$, $X_{\text{H}_2\text{O}} = X_{\text{CO}} = X_{\text{CO}_2} = 25\%$.

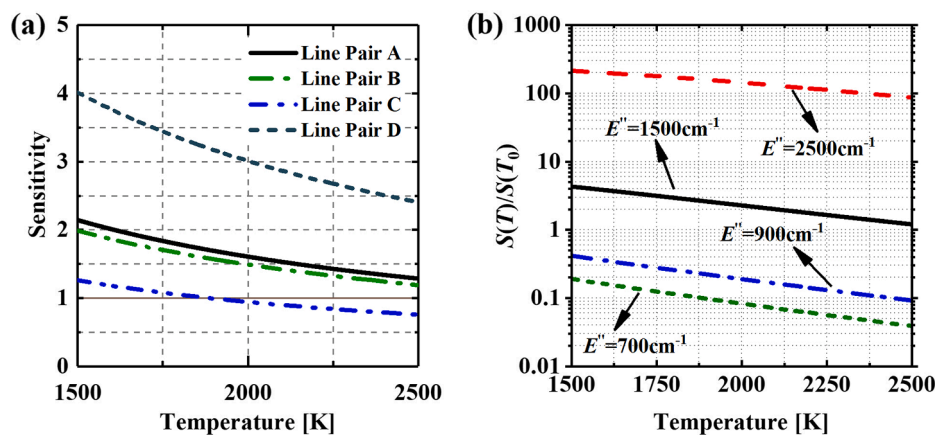


Fig. 3. (a) Temperature sensitivity of four H_2O candidate line pairs in expected temperature range of 1500–2500 K, (b) Simulated line-strength ratio $S(T)/S(T_0)$ for different lower-state energies E'' (700 cm^{-1} , 900 cm^{-1} , 1500 cm^{-1} , and 2500 cm^{-1}) as a function of temperature.

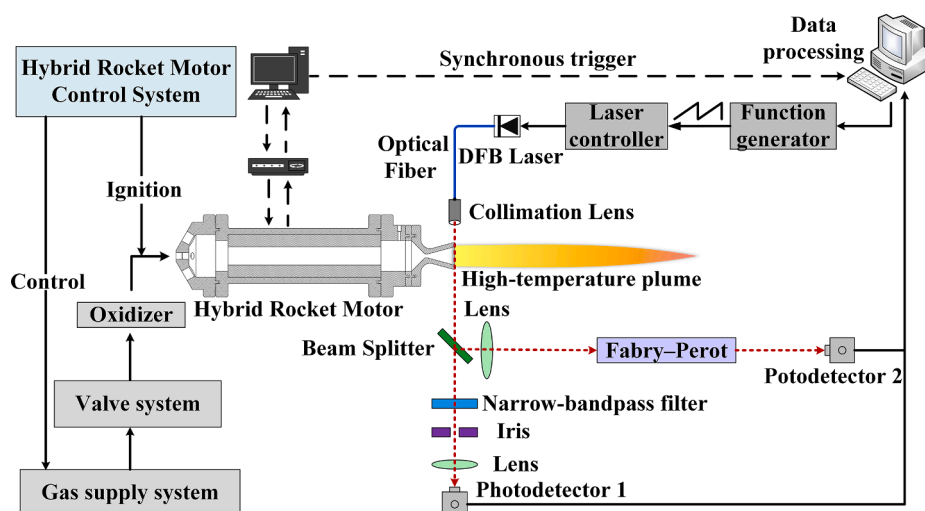


Fig. 4. Schematic of the TDLAS diagnostic system and hybrid rocket motor system.

conducted at different O/F ratios, which are listed in Table 2.

Fig. 4 also illustrates the optical setup of the designed TDLAS system. To probe the selected H_2O transitions, a mid-infrared DFB laser (Nanoplus GmbH) centered near 2.5 μm was deployed with a stable output power of approximately 10 mW. The laser wavelength and intensity were continuously tuned by a commercial laser controller (Thorlabs, model ITC-502). To implement scanned-wavelength DA strategy, the current of the DFB laser was modulated by a ramp signal of 2 kHz provided by a function generator (Tektronix, model AFG-3101) to cover the three transitions of line pair A in Table 1. The output laser beam was collimated to a beam waist diameter of approximately 0.5 mm and located within ~ 0.5 mm of the nozzle exit plane. The transmitted light was then split into two beams. Part of the laser beam passed through a narrow-band filter (with a center wavelength of 2.5 μm and bandwidth of 50 nm) and an iris to mitigate the influence of thermal

radiation. A focusing lens was used to collimate the collected light to further enhance the transmitted signal. The other part of the laser beam was directed into a Fabry-Perot interferometer (Thorlabs, model SA200-18B, 1.5 GHz FSR) to calibrate the absolute wavelength. Finally, these two laser beams were simultaneously collected and monitored by photodetectors (Thorlabs, model PDA10D2), and the detected signals were recorded by a data processing module (National Instruments, model PCIE 6361) at a sampling rate of 2 MHz.

4. Results and discussion

4.1. TDLAS measurement results

Variations of a representative raw data trace (case 5) detected by the TDLAS system are presented in Fig. 5. This trace covers the whole process of motor ignition, combustion, and shutdown. The variations of amplitude intensity in Fig. 5 were mainly caused by the unburned fuel. After the ignition at approximately 0.6 s, solid paraffin was quickly heated and fuel droplets were supplied to the reactive flow. Owing to the diffusive nature of the combustion, part of the paraffin droplets flowed into the exhaust gas before they were burned. These unburned droplets blocked part of the laser intensity by sticking to the optical windows, which was consistent with the sudden drop of the detected signal in the first combustion stage. As the combustion approached a steady state, part of the solid fuel covering the optical windows was heated by the

Table 2
Firing test conditions.

Case	O/F	Mass flux of O_2 [$\text{g}/(\text{cm}^2\cdot\text{s})$]
1	3.11	2.47
2	3.18	2.57
3	3.03	2.78
4	2.77	2.95
5	3.10	3.40

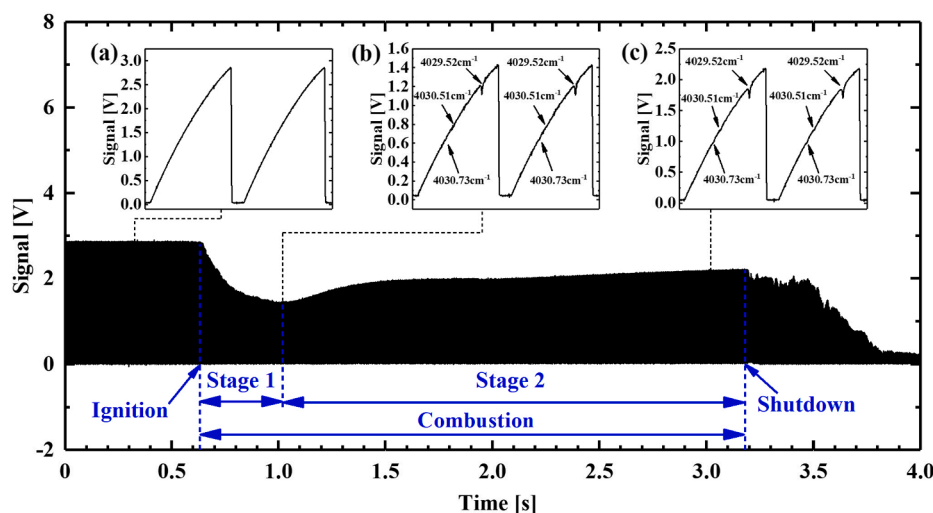


Fig. 5. TDLAS raw data covering the whole process of ignition, combustion and shutdown of the hybrid rocket motor.

high-temperature plume and was finally entrained into the hypersonic flows. Therefore, the signal intensity in the second stage appeared to slowly increase and eventually stabilize. When the motor was shut down, the unburned paraffin began to cover the optical windows after it was cooled down. This explains the fluctuations in signal intensity near 3.2 s. Typical single laser scans of different stages were extracted from the raw data trace. Fig. 5(a) shows that no visible H_2O absorption occurred before motor ignition. Fig. 5(b) is the absorption signal at the lowest amplitude of the raw data trace. Despite the laser attenuation, all the H_2O absorption peaks at 4029.52 cm^{-1} , 4030.51 cm^{-1} and 4030.73 cm^{-1} were still visible, although the latter two peaks were relatively weak. When the signal amplitude increased as shown in Fig. 5(c), these absorption peaks were much clearer than those in Fig. 5(b).

To accurately obtain the temperature and H_2O partial pressure, 50 scans of the sequential raw data were averaged to remove stochastic noise from the laser and plume fluctuation, and the background noise was subtracted to further improve the SNR. A typical 50-scan-averaged signal is shown in Fig. 6(a). Further data processing usually follows this sequence. First, the unattenuated laser intensity I_0 (baseline) was determined by fitting the far wings of each scan using a third-order polynomial. Second, after subtracting the fitted baseline, a Voigt profile was least-squares fitted to the absorption signals. The chosen baseline was adjusted to yield a low fitting residual between the measured data and the Voigt profile. The top panel in Fig. 6(b) shows the measured absorbance covered with the Voigt fit, and the bottom part shows the fitting residuals. The Voigt-fitting residual of less than 1% throughout

the absorption profile indicates that the Voigt profile is suitable for the absorption line shape, and a high SNR has been achieved under this condition. Finally, the fitted line was used to calculate the integrated absorbance A , and hence the line-of-sight static temperature and water vapor partial pressure of the flow can be obtained through Eq. (5) and Eq. (8) respectively.

The four-second variations in measurement results for two representative cases (case 2 and case 3) are shown in Fig. 7. The combustion pressure (obtained by pressure transducers) is also plotted because it reflects the working state of the hybrid rocket motor. For case 2, the first state is from 0 s to ~ 0.5 s, when the oxidizer was injected into the combustion chamber, and hence the combustion pressure P_c , static temperature T , and H_2O partial pressure $P_{\text{H}_2\text{O}}$ in this interval had no sudden changes. When the motor was ignited, a significant ignition pressure peak appeared, and both T and $P_{\text{H}_2\text{O}}$ increased suddenly. During the combustion process (~ 0.5 s to ~ 3.75 s), P_c first increased slowly and stabilized eventually. Both T and $P_{\text{H}_2\text{O}}$ have the same trend as that of P_c . When the motor was shut off, P_c , T , and $P_{\text{H}_2\text{O}}$ all suddenly dropped at 3.75 s. Note that P_c had a slower decrease than T and $P_{\text{H}_2\text{O}}$, which was due to the residual pressure between the combustion chamber and nozzle exit. The working stages of case 3 were similar to those of case 2, but there were differences in chamber pressure P_c . As shown in Fig. 7(a), P_c stabilized at ~ 2.0 s in case 2 but kept increasing until 3.0 s in case 3. These different variations in P_c affected on $P_{\text{H}_2\text{O}}$, which is evident in Fig. 7(b).

The total measurement uncertainties were determined by applying

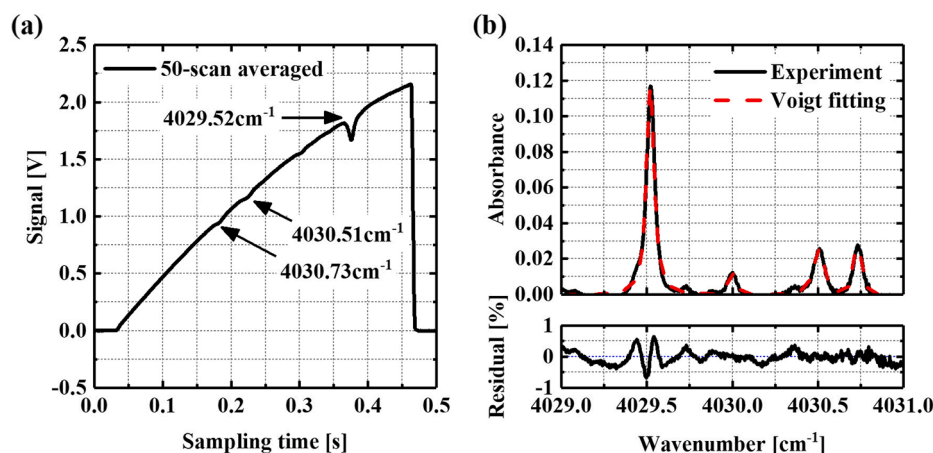


Fig. 6. (a) Representative 50-scan-averaged absorption signals. (b) Typical absorption spectra for temperature and partial pressure measurement. At the top is the experimental absorbance spectrum (black solid line) together with its best-fit Voigt profile (red dash line); the bottom is the corresponding Voigt-fitting residual.

the Taylor series method of uncertainty propagation [47] to the un-

the ANSYS FLUENT CFD software package, as shown in Fig. 8. The

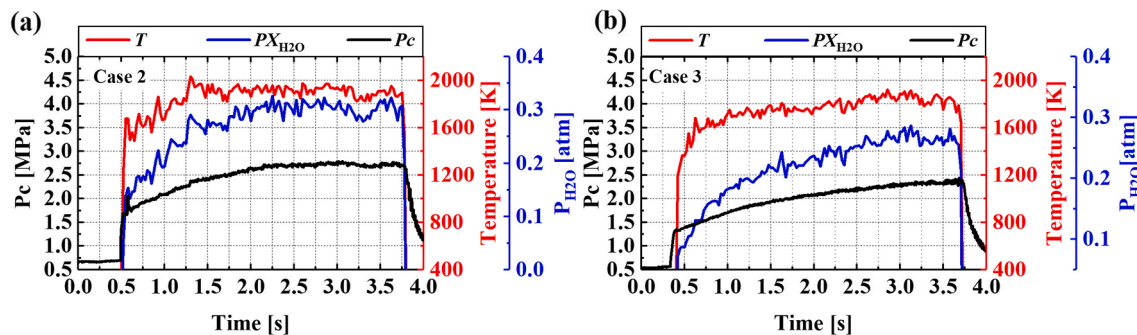
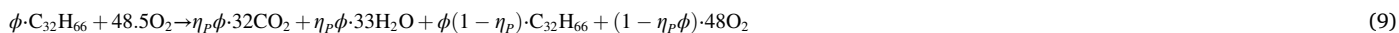


Fig. 7. TDLAS measurements of temperature and H₂O partial pressure for cases 2 (a) and 3 (b) together with chamber pressure variations recorded by the pressure transducer.

certainties in line-strength and temperature. The measured temperature uncertainty determined from the Voigt-fitting residual (less than 1%) and line-strength uncertainty (~2% validated in [12,42,44,45]) is about 2.24%. The temperature uncertainty will propagate to line-strength S as discussed in [43]. Therefore, the uncertainty in the partial pressure $P_{\text{H}_2\text{O}}$ consists of the line-strength uncertainty and Voigt-fitting residual according to Eq. (8). To properly analyze the measurement uncertainty, the static temperatures in Fig. 7 were averaged for each case. The averaged values and calculated uncertainties are listed in Table 3, which indicates that temperature uncertainty has a significant impact on the accuracy of partial pressure measurement. It is important to clarify that the integrated absorbance A in the thermal boundary layer is found to be about two orders of magnitude lower than that in the total optical path length (obtained by a brief calculation), which illustrates that the thermal boundary layer has a small impact on TDLAS measurement results. Thus, it is reasonable to assume that the cross section of the nozzle exit was quasi-uniform, and line-of-sight results were used to represent parameters in the core flow. Considering heat transfer between the core flow and the boundary layer, temperature and species gradients are expected to occur in the nozzle, this may influence the measurement accuracy. In our future study, tunable diode laser absorption tomography (TDLAT) will be utilized to improve measurement spatial resolution (providing a two-dimensional distribution of temperature and species concentration).

4.2. Combustion efficiency evaluation

The combustion efficiency of the hybrid rocket motor was evaluated from the perspectives of chemical equilibrium (using H₂O partial pressure) and heat release (using gas temperature), respectively, and the results were compared with the traditional C^* -based efficiency to validate the evaluation methods. CFD simulations were constructed to obtain the combustion efficiency based on TDLAS measurements; the inlet conditions of the simulations were obtained from the online pro-



gram NASA Chemical Equilibrium with Applications (CEA).

4.2.1. CFD simulations

The combustion process of hybrid rocket motors involves complex physicochemical mechanisms such as multiphase thermochemistry, diffusive mixing and turbulence [12]. To properly simplify the computations, a 2D-axisymmetric model of the nozzle was constructed using

Table 3

Averaged TDLAS results and calculated uncertainties.

Case	\bar{T} (K)	$\bar{P}_{\text{H}_2\text{O}}$ (atm)	$\Delta T/T$	$\Delta S/S$	$\Delta P_{\text{H}_2\text{O}}/P_{\text{H}_2\text{O}}$
1	1870.8	0.279	2.24%	3.43%	3.57%
2	1907.8	0.292	2.24%	3.58%	3.72%
3	1810.6	0.249	2.24%	3.17%	3.32%
4	1926.5	0.253	2.24%	3.66%	3.79%
5	1929.8	0.237	2.24%	3.67%	3.81%

whole model contains about 14,640 cells and 15,047 nodes. The inner space of the nozzle was selected as the calculation domain, and the inlet diameter of the nozzle was 50 mm. The standard $k-\epsilon$ turbulence model with a nonequilibrium wall function was used [48].

The simulations were based on the following assumptions:

- (1) Only gas-phase species were present and no chemical reaction occurred during the compression and expansion of the isentropic flow. This means the concentration and phase of the combustion products remained the same in the nozzle.
- (2) The radiant heat flux was negligible since the fuel is without metal additives [4,7,49], and the convective heat transfer was considered.
- (3) The nozzle walls were adiabatic with no slip conditions, and the temperature was set to 1000 K.

The inlet conditions of the nozzle were obtained from CEA. The CEA and CFD simulation results are listed in Table 4.

4.2.2. $P_{\text{H}_2\text{O}}$ -based combustion efficiency η_p

The combustion efficiency η_p is defined as the mole fraction of the fuel that is completely burned and transferred to CO₂ [50]. According to this definition, the global reaction equation describing the fuel consumption is:

where ϕ is the equivalence ratio. It is noteworthy that Eq. (9) is based on the following assumptions: (1) CO₂ and H₂O are the only combustion products; (2) all the H₂O comes from the chemical reaction.

From Eq. (9), the $P_{\text{H}_2\text{O}}$ -based combustion efficiency η_p can be derived from the relation between the H₂O mole fraction and its pressure

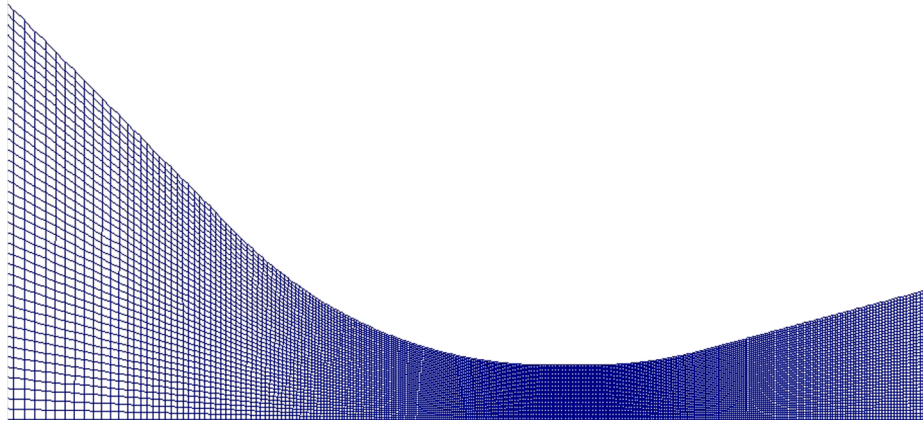


Fig. 8. 2D structured mesh model for the Laval nozzle.

Table 4
CEA and CFD simulation results.

Case	CEA		Fluent		
	T_c^a (K)	γ^b	P_s^c (atm)	T_s^d (K)	v^e (m/s)
1	3530.3	1.13	0.592	1786.5	2335.3
2	3534.0	1.13	0.620	1791.4	2333.9
3	3509.9	1.13	0.506	1770.0	2330.5
4	3514.9	1.13	0.517	1767.3	2346.8
5	3498.9	1.12	0.478	1761.9	2321.6

^a T_c is the adiabatic combustion temperature in the chamber.

^b γ is the specific heat ratio.

^c P_s is the static pressure at the nozzle exit.

^d T_s is the static temperature at the nozzle exit.

^e v is the velocity magnitude at the nozzle exit.

fraction:

$$\eta_p = \frac{48.5/\phi + 1}{33P_s/P_{H_2O} - 15.5} \quad (10)$$

where the static pressure P_s at the nozzle exit is obtained from Fluent simulations (as shown in Table 4). The evaluation results for the five cases were 82.7%, 84.1%, 85.2%, 77.2%, and 87.5%.

4.2.3. T -based Combustion efficiency η_T

Because temperature is an important parameter reflecting the heat release of combustion systems, the total temperature was used to evaluate the combustion efficiency η_T through the following formula

$$\eta_T = \frac{T_e - T_{O_2}}{T_c - T_{O_2}} \quad (11)$$

where T_{O_2} is the total temperature of the oxygen, T_c is the adiabatic combustion temperature as mentioned previously, and T_e represents the actual total temperature, which was calculated through the isentropic

Table 5
Combustion efficiencies.

Case	O/F	G_{ox}^a [g / (cm ² ·s)]	η_p	η_T	$\eta_{C^*}^b$
1	3.11	2.47	82.7%	84.9%	76.7%
2	3.18	2.57	84.1%	85.9%	77.7%
3	3.03	2.78	85.2%	83.4%	78.1%
4	2.77	2.95	77.2%	87.4%	73.9%
5	3.10	3.40	87.5%	84.6%	80.7%

^a G_{ox} is the mass flux of the oxidizer.

^b η_{C^*} is calculated through the traditional method using characteristic velocity, and the theoretical value of C^* is obtained from CEA results.

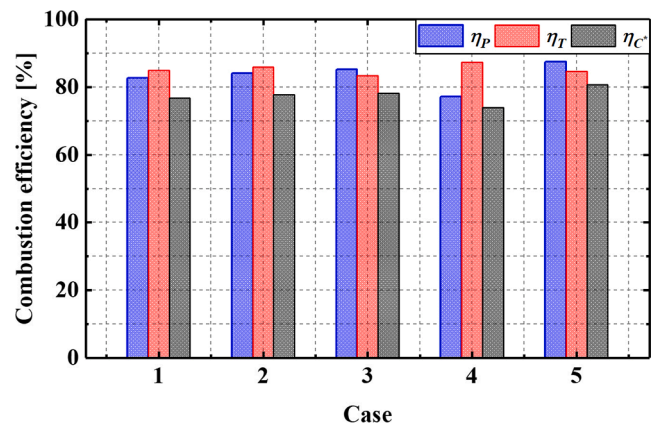


Fig. 9. Combustion efficiencies evaluated through H_2O partial pressure, total temperature, and characteristic velocity of the hybrid rocket motor.

flow equation

$$T_e = \left(1 + \frac{\gamma - 1}{2} Ma^2\right) T \quad (12)$$

where Ma is the Mach number of the flow at the nozzle exit (derived from Fluent simulations). The evaluation results for the five cases were 84.9%, 85.9%, 83.4%, 87.4%, and 84.6%.

4.2.4. Comparisons with C^* -based efficiency

The evaluated combustion efficiencies for all the cases and firing conditions are summarized in Table 5 and visualized in Fig. 9 for further analysis and discussion.

According to Fig. 9, the P_{H_2O} -based efficiency shows the same trend with respect to the C^* -based efficiency, and the differences between them are constrained to 3–7%. This validates the ability of this method to evaluate the combustion performance of hybrid rocket motors. However, the T -based efficiency is not aligned with the C^* -based efficiency. Note that η_T is much bigger than η_{C^*} for all the cases. This observation is possibly due to the assumption of non-combustion in the isentropic flow through the nozzle. Neglecting combustion in the nozzle flow yields lower adiabatic temperature at the nozzle exit, therefore, the evaluated efficiency η_T becomes higher when the combustion was neglected (according to Eq. (11)). The following analysis related to combustion performances is based on η_p and η_{C^*} .

It is noteworthy that, except for case 4, both η_p and η_{C^*} become higher from case 1 to case 5 with oxidizer mass flux increasing from 2.47 to 3.40 g / (cm²·s). Such increasing trend agrees with the theoretical

understanding of droplet entrainment [51]. For paraffin fuels, a liquid layer forms when the solid surface is heated. When the oxidizer flows at high speed over the melting surface of the fuel, tiny droplets are produced and supplied to the reaction zone. Therefore, when the mass flux of the oxidizer flow increases, the droplet size decreases, leading to better mixing with the oxidizer flow and hence higher combustion efficiency [52]. For case 4, however, η_p and η_{C^*} are significantly lower than that of case 3 even the oxidizer mass flux increases. This observation is due to the lower O/F ratio in case 4, which suggests less efficient fuel–oxidizer mixing for the combustion process of hybrid motor [51,53].

Overall, the combustion efficiency of a hybrid rocket motor has been evaluated through TDLAS measurements, and the results presented above demonstrate that TDLAS technology can provide insights into the physicochemical mechanisms that govern the overall combustion performance of hybrid rocket motors. However, the current work still needs to be improved to achieve further understanding of the multi-phase combustion physics of hybrids. Our work would be further optimized by considering that the O/F ratio changes over time during the combustion of hybrid rocket motors [54]. The ultrasonic pulse echo technique allows sequential measurement to determine the local instantaneous regression rate of solid fuels [55,56]. We envision that time-resolved diagnosis of motor combustion efficiency can be achieved if the TDLAS measurement in this work is combined with the ultrasonic pulse echo technique. Additionally, we expect to optimize the CFD model to take chemical reactions into consideration, and to construct a three-dimensional model to improve the simulation accuracy. Furthermore, to improve measurement accuracy and spatial resolution, tunable diode laser absorption tomography (TDLAT) will be applied to determine two-dimensional distributions of temperature and species concentration.

5. Conclusions

This work has detailed experimental research on characterizing combustion of a laboratory-scale oxygen/paraffin hybrid rocket motor. Experiments were conducted at different oxidizer mass fluxes ranging from 2.47 to 3.40 g/(cm²·s), corresponding to O/Fs ranging from 2.77 to 3.18. Variations in temperature and H₂O partial pressure were measured by a mid-infrared TDLAS system near 2.5 μm, which covered the whole process of motor ignition, combustion, and shutdown. Analysis of uncertainty propagation found temperature uncertainty has a significant impact on partial pressure accuracy. A 2D model was constructed using the ANSYS FLUENT CFD software package. The TDLAS results were combined with CFD simulations to evaluate the combustion efficiency of the motor, for which the inlet conditions were provided by the CEA results. The evaluated P_{H2O}-based efficiency η_p agrees well with the traditional C*-based η_{C^*} , which validates the effectiveness of this evaluation method. However, the evaluated T-based efficiency η_T was not consistent with η_{C^*} , which may be due to the assumption of non-combustion in the CFD simulations. Comparing η_T and η_{C^*} among different firing cases, it was found that a higher oxidizer mass flux or O/F ratio can improve the combustion performance, which agrees with droplet entrainment theory. These results validated the feasibility of TDLAS technology for combustion characterization of hybrid rocket motors, and suggestions were proposed for further studies. It is envisioned that TDLAS technology has the potential to inform design considerations of hybrid rocket motors.

CRedit authorship contribution statement

Sihan Fang: Conceptualization, Software, Formal analysis, Investigation, Writing - original draft, Writing - review & editing, Visualization. **Zezhong Wang:** Software, Formal analysis, Investigation, Visualization. **Xin Lin:** Methodology, Software, Formal analysis, Investigation, Visualization, Funding acquisition. **Fei Li:** Methodology, Software,

Visualization, Funding acquisition. **Renjie Li:** Investigation. **Jing Li:** Conceptualization. **Zhedian Zhang:** Methodology, Supervision. **Yan Liu:** Methodology. **Xilong Yu:** Methodology, Software, Supervision, Funding acquisition.

Declaration of Competing Interest

The authors declare that they have no known competing financial interests or personal relationships that could have appeared to influence the work reported in this paper.

Acknowledgements

This work was funded in part by the National Natural Science Foundation of China (No. 11802315, No. 11872368, No. 12072355 and No. 11927803), Equipment Pre-research Foundation of National Defense Key Laboratory (No. 6142701190402), and Design Study of Hydrogen-Rich Fuel Production, HAT Characteristics and Specific Test Applications in HIGT (No. BM2019001).

References

- [1] G. Cai, Z. Zhao, B. Zhao, et al., Regression rate and combustion performance investigation on hybrid rocket motor with head-end swirl injection under high geometric swirl number, *Aerosp. Sci. Technol.* 103 (2020), 105922, <https://doi.org/10.1016/j.ast.2020.105922>.
- [2] H. Tian, Y. Duan, H. Zhu, Three-dimensional numerical analysis on combustion performance and flow of hybrid rocket motor with multi-segmented grain, *Chin. J. Aeronaut.* 33 (2020) 1181–1191, <https://doi.org/10.1016/j.cja.2019.12.021>.
- [3] Y. Wu, Z. Zhang, F. Liang, N. Wang, Combustion characterization of a CH₄/O₂ rapid mixed swirl torch igniter for hybrid rocket motors, *Aerosp. Sci. Technol.* 98 (2020), 105666, <https://doi.org/10.1016/j.ast.2019.105666>.
- [4] H. Tian, L. He, H. Zhu, et al., Numerical and experimental investigation on hybrid rocket motor with two-hole segmented rotation grain, *Aerosp. Sci. Technol.* 92 (2019) 820–830, <https://doi.org/10.1016/j.ast.2019.07.006>.
- [5] B. Vignesh, R. Kumar, Effect of multi-location swirl injection on the performance of hybrid rocket motor, *Acta Astronaut.* 176 (2020) 111–123, <https://doi.org/10.1016/j.actaastro.2020.06.029>.
- [6] L. Galfetti, F. Nasuti, D. Pastrone, A.M. Russo, An Italian network to improve hybrid rocket performance: Strategy and results, *Acta Astronaut.* 96 (2014) 246–260, <https://doi.org/10.1016/j.actaastro.2013.11.036>.
- [7] H. Tian, X. Sun, Y. Guo, P. Wang, Combustion characteristics of hybrid rocket motor with segmented grain, *Aerosp. Sci. Technol.* 46 (2015) 537–547, <https://doi.org/10.1016/j.ast.2015.08.009>.
- [8] C. Li, G. Cai, H. Tian, Numerical analysis of combustion characteristics of hybrid rocket motor with multi-section swirl injection, *Acta Astronaut.* 123 (2016) 26–36, <https://doi.org/10.1016/j.actaastro.2016.02.023>.
- [9] Y.S. Chen, T.H. Chou, B.R. Gu, et al., Multiphysics simulations of rocket engine combustion, *Comput. Fluids* 45 (2011) 29–36, <https://doi.org/10.1016/j.compfluid.2010.09.010>.
- [10] B. Adrian-Nicolae, Performances Study of a Hybrid Rocket Engine, *INCAS BULLETIN* 10 (2018) 173–184, <https://doi.org/10.13111/2066-8201.2018.10.2.16>.
- [11] Y. Li, C. Hu, X. Zhu, et al., Experimental study on combustion characteristics of powder magnesium and carbon dioxide in rocket engine, *Acta Astronaut.* 155 (2019) 334–349, <https://doi.org/10.1016/j.actaastro.2018.11.006>.
- [12] F.A. Bendana, I.C. Sanders, J.J. Castillo, et al., In-situ thermochemical analysis of hybrid rocket fuel oxidation via laser absorption tomography of CO, CO₂, and H₂O, *Exp. Fluids* 61 (2020) 190, <https://doi.org/10.1007/s00348-020-03004-7>.
- [13] C.H. Smith, C.S. Goldenstein, R.K. Hanson, A scanned-wavelength-modulation absorption-spectroscopy sensor for temperature and H₂O in low-pressure flames, *Meas. Sci. Technol.* 25 (2014), 115501, <https://doi.org/10.1088/0957-0233/25/11/115501>.
- [14] L. Ma, X. Li, S.T. Sanders, et al., 50-kHz-rate 2D imaging of temperature and H₂O concentration at the exhaust plane of a J85 engine using hyperspectral tomography, *Opt. Express* 21 (2013) 1152–1162, <https://doi.org/10.1364/OE.21.001152>.
- [15] S. Roy, J. Gord, A. Patnaik, Recent advances in coherent anti-Stokes Raman scattering spectroscopy: Fundamental developments and applications in reacting flows, *Prog. Energy Combust. Sci.* 36 (2010) 280–306, <https://doi.org/10.1016/j.pecs.2009.11.001>.
- [16] C. Dennis, B. Bojko, On the combustion of heterogeneous AP/HTPB composite propellants: A review, *Fuel* 254 (2019), 115646, <https://doi.org/10.1016/j.fuel.2019.115646>.
- [17] S. Li, A. Farooq, R.K. Hanson, H₂O temperature sensor for low-pressure flames using tunable diode laser absorption near 2.9 μm, *Meas. Sci. Technol.* 22 (2011), 125301, <https://doi.org/10.1088/0957-0233/22/12/125301>.
- [18] T. Cai, G. Wang, Z. Cao, et al., Sensor for headspace pressure and H₂O concentration measurements in closed vials by tunable diode laser absorption

- spectroscopy, *Opt. Laser. Eng.* 58 (2014) 48–53, <https://doi.org/10.1016/j.optlaseng.2013.12.005>.
- [19] X. Guo, F. Zheng, C. Li, et al., A portable sensor for in-situ measurement of ammonia based on near-infrared laser absorption spectroscopy, *Opt. Laser. Eng.* 115 (2019) 243–248, <https://doi.org/10.1016/j.optlaseng.2018.12.005>.
- [20] G. Zhang, G. Wang, Y. Huang, et al., Reconstruction and simulation of temperature and CO₂ concentration in an axisymmetric flame based on TDLAS, *Opt. 170* (2018) 166–177, <https://doi.org/10.1016/j.jileo.2018.05.123>.
- [21] Z. Wang, Y. Deguchi, T. Kamimoto, et al., Pulverized coal combustion application of laser-based temperature sensing system using computed tomography – Tunable diode laser absorption spectroscopy (CT-TDLAS), *Fuel* 268 (2020), 117370, <https://doi.org/10.1016/j.fuel.2020.117370>.
- [22] A.G. Hendricks, U. Vandsburger, The effect of fuel composition on flame dynamics, *Exp. Therm Fluid Sci.* 32 (2007) 126–132, <https://doi.org/10.1016/j.expthermflusci.2007.02.007>.
- [23] L. Ma, K.-P. Cheong, H. Ning, W. Ren, An improved study of the uniformity of laminar premixed flames using laser absorption spectroscopy and CFD simulation, *Exp. Therm Fluid Sci.* 112 (2020), 110013, <https://doi.org/10.1016/j.expthermflusci.2019.110013>.
- [24] I.A. Schultz, C.S. Goldenstein, J.B. Jeffries, et al., Diode Laser Absorption Sensor for Combustion Progress in a Model Scramjet, *J. Propul. Power* 30 (2014) 550–557, <https://doi.org/10.2514/1.B34905>.
- [25] G.B. Rieker, H. Li, X. Liu, et al., Rapid measurements of temperature and H₂O concentration in IC engines with a spark plug-mounted diode laser sensor, *Proc. Combust. Inst.* 31 (2007) 3041–3049, <https://doi.org/10.1016/j.proci.2006.07.158>.
- [26] C.S. Goldenstein, R.M. Spearrin, J.B. Jeffries, R.K. Hanson, Infrared laser absorption sensors for multiple performance parameters in a detonation combustor, *Proc. Combust. Inst.* 35 (2015) 3739–3747, <https://doi.org/10.1016/j.proci.2014.05.027>.
- [27] K. Sun, R. Sur, X. Chao, et al., TDL absorption sensors for gas temperature and concentrations in a high-pressure entrained-flow coal gasifier, *Proc. Combust. Inst.* 34 (2013) 3593–3601, <https://doi.org/10.1016/j.proci.2012.05.018>.
- [28] A.K. Mohamed, J. Messineo, J.-Y. Lestrade, et al., Tunable diode laser absorption spectroscopy of CO₂ and H₂O at 2.7 μm in a scramjet combustor and in exhaust gases of a hybrid rocket motor, in: 32nd AIAA Aerodynamic Measurement Technology and Ground Testing Conference, American Institute of Aeronautics and Astronautics, Washington, D.C., 2016, <https://doi.org/10.2514/6.2016-3548>.
- [29] M.A. Bolshov, Y.A. Kuritsyn, Y.V. Romanovskii, Tunable diode laser spectroscopy as a technique for combustion diagnostics, *Spectrochim. Acta, Part B* 106 (2015) 45–66, <https://doi.org/10.1016/j.sab.2015.01.010>.
- [30] C.S. Goldenstein, R.M. Spearrin, J.B. Jeffries, R.K. Hanson, Infrared laser-absorption sensing for combustion gases, *Prog. Energy Combust. Sci.* 60 (2017) 132–176, <https://doi.org/10.1016/j.pecs.2016.12.002>.
- [31] X. Zhou, J.B. Jeffries, R.K. Hanson, Development of a fast temperature sensor for combustion gases using a single tunable diode laser, *Appl. Phys. B* 81 (2005) 711–722, <https://doi.org/10.1007/s00340-005-1934-y>.
- [32] X. Chao, J.B. Jeffries, R.K. Hanson, Absorption sensor for CO in combustion gases using 2.3 μm tunable diode lasers, *Meas. Sci. Technol.* 20 (2009), <https://doi.org/10.1088/0957-0233/20/11/115201>.
- [33] A. Farooq, J.B. Jeffries, R.K. Hanson, In situ combustion measurements of H₂O and temperature near 2.5 μm using tunable diode laser absorption, *Meas. Sci. Technol.* 19 (2008), 075604, <https://doi.org/10.1088/0957-0233/19/7/075604>.
- [34] X. Liu, *Line-of-sight absorption of H₂O vapor: gas temperature sensing in uniform and nonuniform flows*, Stanford University, California, 2006.
- [35] R. Gao, S. O'byrne, J.-L. Liow, T.K. Boyson, An experimental study of pressure distribution nonlinearity in a circular micro-tube, *Exp. Therm Fluid Sci.* 97 (2018) 468–483, <https://doi.org/10.1016/j.expthermflusci.2018.05.020>.
- [36] W.Y. Peng, S.J. Cassady, C.L. Strand, et al., Single-ended mid-infrared laser-absorption sensor for time-resolved measurements of water concentration and temperature within the annulus of a rotating detonation engine, *Proc. Combust. Inst.* 37 (2019) 1435–1443, <https://doi.org/10.1016/j.proci.2018.05.021>.
- [37] M.P. Arroyo, R.K. Hanson, Absorption measurements of water-vapor concentration, temperature, and line-shape parameters using a tunable InGaAsP diode laser, *Appl. Opt.* 32 (1993) 6104–6116, <https://doi.org/10.1364/AO.32.006104>.
- [38] I.E. Gordon, L.S. Rothman, C. Hill, et al., The HITRAN2016 molecular spectroscopic database, *J. Quant. Spectrosc. Radiat. Transfer* 203 (2017) 3–69, <https://doi.org/10.1016/j.jqsrt.2017.06.038>.
- [39] L.S. Rothman, I.E. Gordon, R.J. Barber, et al., HITEMP, the high-temperature molecular spectroscopic database, *J. Quant. Spectrosc. Radiat. Transfer* 111 (2010) 2139–2150, <https://doi.org/10.1016/j.jqsrt.2010.05.001>.
- [40] G. Li, I. Gordon, L. Rothman, et al., Rovibrational Line Lists for Nine Isotopologues of the CO Molecule in the X¹Σ⁺ Ground Electronic State, *The Astrophysical Journal Supplement Series* 216 (2015) 15, <https://doi.org/10.1088/0067-0049/216/1/15>.
- [41] L. Ma, H. Ning, J. Wu, W. Ren, In situ flame temperature measurements using a mid-infrared two-line H₂O laser-absorption thermometry, *Combust. Sci. Technol.* 190 (2018) 392–407, <https://doi.org/10.1080/00102202.2017.1392515>.
- [42] C.S. Goldenstein, I.A. Schultz, R.M. Spearrin, et al., Scanned-wavelength-modulation spectroscopy near 2.5 μm for H₂O and temperature in a hydrocarbon-fueled scramjet combustor, *Appl. Phys. B* 116 (2014) 717–727, <https://doi.org/10.1007/s00340-013-5755-0>.
- [43] C. Wei, D.I. Pineda, L. Paxton, et al., Mid-infrared laser absorption tomography for quantitative 2D thermochemistry measurements in premixed jet flames, *Appl. Phys. B* 124 (2018) 123, <https://doi.org/10.1007/s00340-018-6984-z>.
- [44] C.S. Goldenstein, J.B. Jeffries, R.K. Hanson, Diode laser measurements of lineshape and temperature-dependent lineshape parameters of H₂O-, CO₂-, and N₂-perturbed H₂O transitions near 2474 and 2482nm, *J. Quant. Spectrosc. Radiat. Transfer* 130 (2013) 100–111, <https://doi.org/10.1016/j.jqsrt.2013.06.008>.
- [45] C.S. Goldenstein, I.A. Schultz, J.B. Jeffries, R.K. Hanson, Two-color absorption spectroscopy strategy for measuring the column density and path average temperature of the absorbing species in nonuniform gases, *Appl. Opt.* 52 (2013) 7950–7962, <https://doi.org/10.1364/AO.52.007950>.
- [46] Z. Wang, X. Lin, F. Li, X. Yu, Combustion performance of a novel hybrid rocket fuel grain with a nested helical structure, *Aerosp. Sci. Technol.* 97 (2020), 105613, <https://doi.org/10.1016/j.ast.2019.105613>.
- [47] W.C. Hugh, W.S. Glenn, *Experimentation, validation, and uncertainty analysis for engineers*, John Wiley & Sons, John Wiley & Sons, 2018.
- [48] N. Bellomo, M. Lazzarin, F. Barato, M. Grosse, Numerical Investigation of the Effect of a Diaphragm on the Performance of a Hybrid Rocket Motor, 46th AIAA/ASME/SAE/ASEE Joint Propulsion Conference & Exhibit, American Institute of Aeronautics and Astronautics (2010), <https://doi.org/10.2514/6.2010-7033>.
- [49] G. Cai, B. Cao, H. Zhu, et al., Parametric investigation of secondary injection in post-chamber on combustion performance for hybrid rocket motor, *Acta Astronaut.* 140 (2017) 427–438, <https://doi.org/10.1016/j.actaastro.2017.09.009>.
- [50] F. Li, X. Yu, H. Gu, et al., Simultaneous measurements of multiple flow parameters for scramjet characterization using tunable diode-laser sensors, *Appl. Opt.* 50 (2011) 6697–6707, <https://doi.org/10.1364/AO.50.006697>.
- [51] A. Karabeyoglu, G. Zilliac, B.J. Cantwell, et al., Scale-Up Tests of High Regression Rate Paraffin-Based Hybrid Rocket Fuels, *J. Propul. Power*, American Institute of Aeronautics and Astronautics (2004), <https://doi.org/10.2514/1.3340>.
- [52] T. Ishiguro, K. Sinohara, K. Sakio, I. Nakagawa, A Study on Combustion Efficiency of a Paraffin-based Hybrid Rockets, 47th AIAA/ASME/SAE/ASEE Joint Propulsion Conference & Exhibit, American Institute of Aeronautics and Astronautics (2011), <https://doi.org/10.2514/6.2011-5679>.
- [53] S. Oyama, Y. Hirata, K. Araki, et al., Effects of Multi-Section Swirl Injection Method on Fuel Regression Rate of High Density Polyethylene Fueled Hybrid Rocket Engine, 49th AIAA/ASME/SAE/ASEE Joint Propulsion Conference, American Institute of Aeronautics and Astronautics (2013), <https://doi.org/10.2514/6.2013-4040>.
- [54] A.M. Karabeyoglu, B.J. Evans, Effect of “O/F Shift” on Combustion Efficiency, 50th AIAA/ASME/SAE/ASEE Joint Propulsion Conference, American Institute of Aeronautics and Astronautics (2014), <https://doi.org/10.2514/6.2014-3851>.
- [55] F. Dijkstra, P. Korting, R. Van Den Berg, Ultrasonic regression rate measurement in solid fuel ramjets, 26th Joint Propulsion Conference, American Institute of Aeronautics and Astronautics (1990), <https://doi.org/10.2514/6.1990-1963>.
- [56] T. Boardman, L. Porter, F. Brasfield, T. Abel, An ultrasonic fuel regression rate measurement technique for mixture ratio control of a hybrid motor, 31st Joint Propulsion Conference and Exhibit, American Institute of Aeronautics and Astronautics (1995), <https://doi.org/10.2514/6.1995-3081>.